# Supplementary Information：

## Supplementary Section S1

## Comparative evaluation of underwater imaging modalities

A functional comparison of representative underwater imaging modalities is summarized in Supplementary Table S1. Among the compared modalities, LuDAR uniquely combines strong turbidity tolerance, optical absorption-based contrast, and full 3D imaging capability.

| Imaging Modality | Turbidity Tolerance | Lateral Resolution | Ranging Resolution | 3D Imaging | Optical Contrast |
|---|---|---|---|---|---|
| **Optical Camera Imaging** | Low | High | N/A | No | Yes(reflection) |
| **Polarization Imaging** | Medium | High | N/A | No | Yes(reflection) |
| **LiDAR** | Medium | Medium | Medium | Yes | Yes(reflection) |
| **Sonar** | High | Low | Low | Yes | No |
| **LuDAR** | High | Medium | High | Yes | Yes(absorption) |

**Table S1 | Comparative evaluation of underwater imaging modalities.** The table summarizes turbidity tolerance, lateral resolution, contrast mechanism, and 3D imaging capability for optical camera imaging, polarization imaging, LiDAR, and LuDAR.

## Supplementary Section S2

## Calibration of the optical scanning geometry

The galvanometer scanner was first calibrated such that input commands ($x_{in}$, $y_{in}$) corresponded to the actual laser-spot coordinates on the focal plane. A schematic illustration of an uncorrected scan is shown in Fig. S2a. After calibration, a square grid pattern (4 mm pitch) was raster-scanned over a 72×72 point array with 1 mm spacing. A single-element transducer was used to acquire the LU signals; the maximum amplitude from each waveform was extracted, reshaped, and binarized with a fixed threshold to form the image in Fig. S2b. The straight, evenly spaced grid lines confirm accurate pointing fidelity at the focal plane.

The mapping from galvanometer input to optical ray trajectories was established by measuring laser-spot positions at two depths (z = 0 and z = 10 mm) for a set of input commands. The resulting two-dimensional maps of the ray slope components $m_x(x_{in}, y_{in})$ and $m_y(x_{in}, y_{in})$are presented in Fig. S2c and Fig. S2d, respectively.

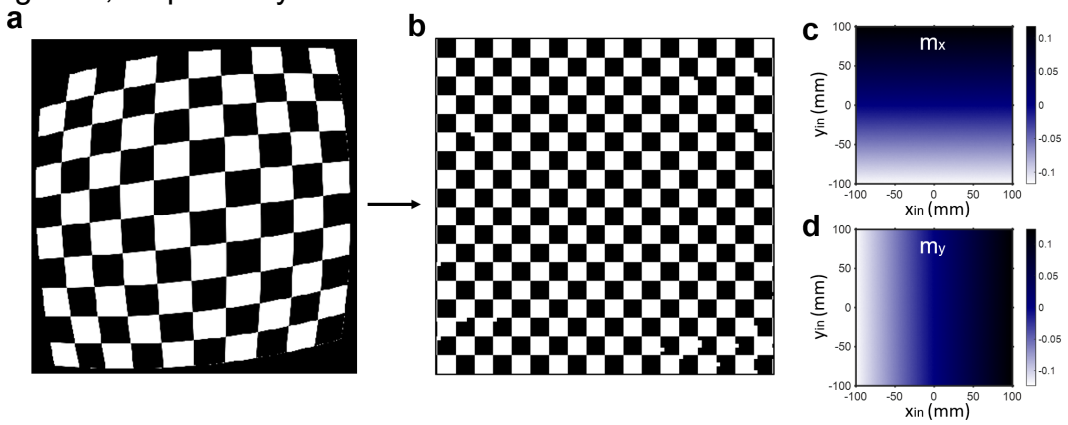


**Fig. S2 | Calibration of the optical scanning geometry. a,** Schematic illustration of an uncorrected scan, showing typical geometric distortion and drift. **b,** Experimental scan of a square grid pattern after calibration. **c,** Two-dimensional map of the ray slope component $m_x$ as a function of input coordinates ($x_{in}$, $y_{in}$). **d,** Corresponding map of the ray slope component $m_y$.

## Supplementary Section S3

## Transducer array pose calibration

The spatial positions and orientations of the eight transducers were calibrated by raster-scanning an aluminum plate at the focal plane over a 30×30 grid with 2 mm spacing. Fig. S3a compares the measured source-detector distances (blue solid lines) with those reconstructed from the fitted transducer positions (red dashed lines) for a representative subset of scan points (indices 100-200). The acoustic axis of each transducer was taken as the direction from its fitted position to the point of maximum amplitude on the focal plane. The calibrated pose parameters, comprising the spatial coordinates ($x_i$, $y_i$, $z_i$) and acoustic axis direction vector ($n_{x,i}$, $n_{y,i}$, $n_{z,i}$) for the i-th transducer, are listed in Supplementary Table S2. A schematic 3D visualization is provided in Fig. S3b.

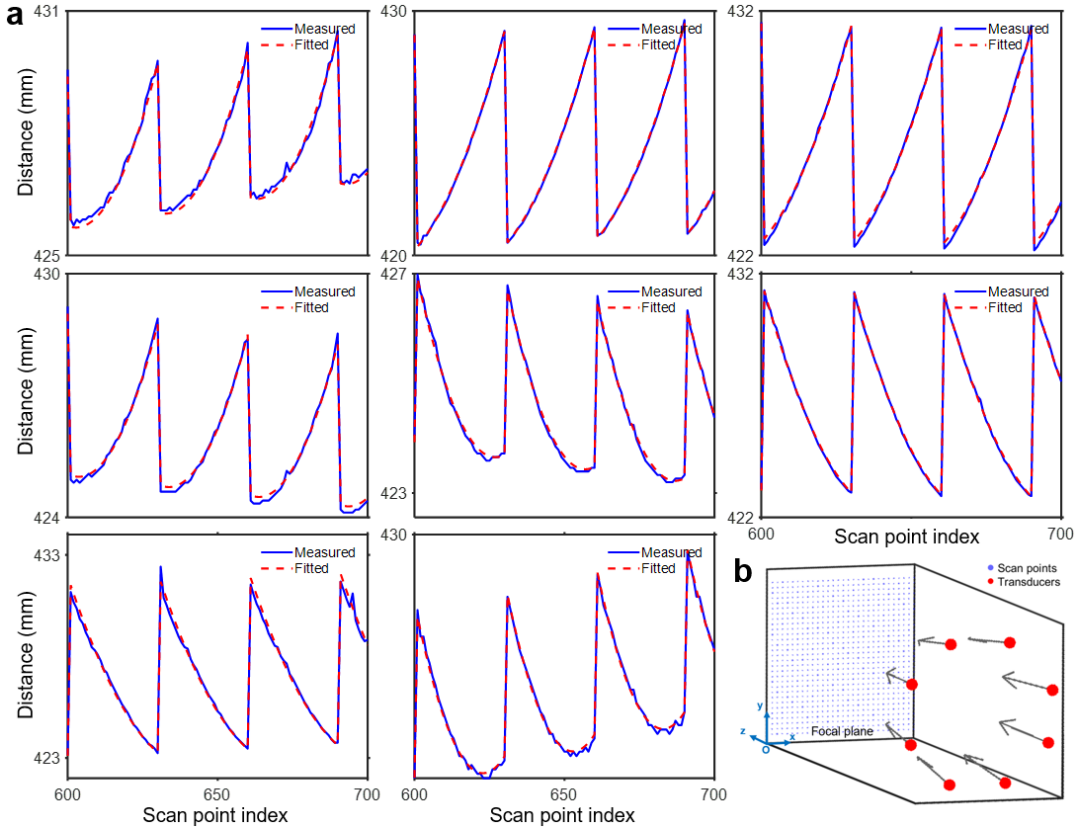


**Fig. S3 | Calibration of the transducer array pose. a,** Measured (blue) and fitted (red dashed) source-detector distance profiles for the eight transducers over scan indices 100-200. **b,** Schematic 3D visualization of the calibrated transducer positions (spheres) and acoustic axis direction vectors (arrows). Numerical values are given in Supplementary Table S2.

| Transducer | x(mm) | y(mm) | z(mm) | $n_x$ | $n_y$ | $n_z$ |
|---|---|---|---|---|---|---|
| 1 | -25.4784 | 51.0087 | -420.3875 | 0.0428 | -0.0856 | 0.9954 |
| 2 | -55.3626 | 17.6803 | -418.2512 | 0.0982 | -0.0213 | 0.9949 |
| 3 | -55.1035 | -27.4437 | -421.3717 | 0.0966 | 0.0480 | 0.9942 |
| 4 | -23.4841 | -58.3251 | -421.9190 | 0.0370 | 0.1052 | 0.9938 |
| 5 | 22.7764 | -56.9774 | -420.3128 | -0.0353 | 0.1020 | 0.9942 |
| 6 | 52.4420 | -26.8026 | -421.9069 | -0.0892 | 0.0462 | 0.9949 |
| 7 | 52.1763 | 20.0950 | -421.1963 | -0.0887 | -0.0278 | 0.9957 |
| 8 | 14.6931 | 54.3212 | -420.1642 | -0.0130 | -0.0949 | 0.9954 |

**Table S2 | Calibrated pose parameters of the eight-element transducer array.** Coordinates (x,y,z) are in millimeters; acoustic axis direction vectors ($n_x$, $n_y$, $n_z$) are normalized unit vectors.

## Supplementary Section S4

## Numerical derivation of the transducer weight function

The single-element transducers used in this work are circular piston transducers with a diameter of 10mm and a centre frequency $f_c = 1\mathrm{MHz}$. The angular directivity of a circular piston in the far field (Fraunhofer region) is given by the normalized pressure distribution

$$D(\theta) = \left|\frac{2J_1(kasin\theta)}{kasin\theta}\right| \quad (S1)$$

where $J_1$ is the first-order Bessel function of the first kind, $k = 2\pi f_c/c$ is the wavenumber at the centre frequency, and $\theta$ is the angle measured from the acoustic axis ($\theta = 0°$ corresponds to normal incidence). The far-field condition is satisfied for distances $r \gg a^2/\lambda$ here $a^2/\lambda \approx 16.7\mathrm{mm}$ at 1 MHz, which is well below the typical working distance (50 cm) in our experiments. The weight applied to each channel is directly taken as the directivity value at the corresponding angle, i.e., $w(\theta) = D(\theta)$. The function $w(\theta)$ was pre-computed numerically on a dense grid of $\theta$ from $0°$ to $90°$ with a step of $0.1°$, as shown in Fig. S4.

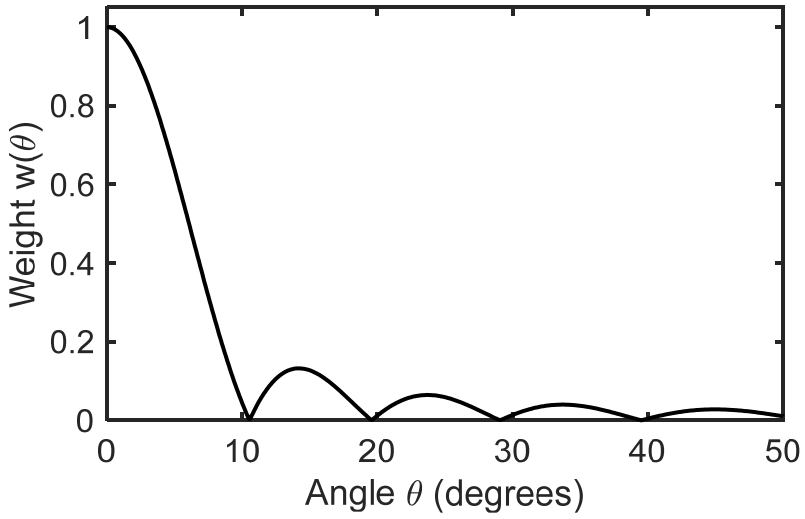


**Fig. S4 | Weight function $w(\theta)$ of the 10 mm diameter, 1 MHz circular piston transducer.** The weight is normalized to unity at $\theta = 0°$(acoustic axis) and is shown for angles from 0° to 50°.

## Supplementary Section S5

## USAF 1951 resolution target

A standard USAF 1951 resolution target was used for qualitative comparison between LuDAR and conventional underwater optical imaging. A photograph of the target is shown in Fig. S5, with a 1 mm scale bar included for reference.

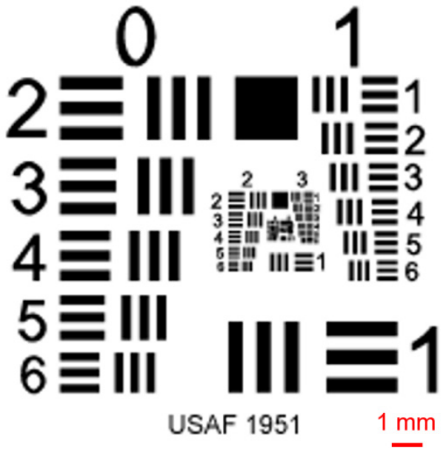


**Fig. S5 | Photograph of the USAF 1951 resolution target.** The scale bar indicates 1 mm.

## Supplementary Section S6

## Deviation distributions across turbidity levels

Deviation histograms for the dolphin model acquired at 20, 23, 25, 27, 30, and 33 NTU are shown in Fig. S6a-f. The histogram for 25 NTU corresponds to Fig. 4f of the main text.

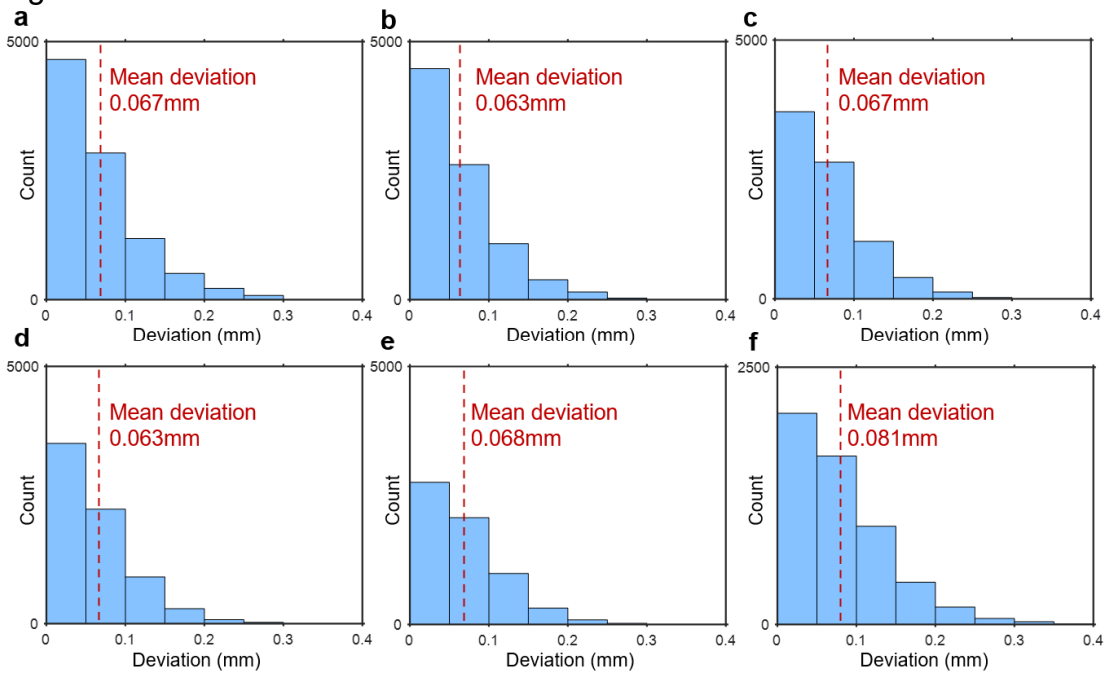


**Fig. S6 |** Histograms of per-point deviations between the reconstructed point cloud and the reference point cloud at turbidities of **a,** 20 NTU, **b,** 23 NTU, **c,** 25 NTU, **d,** 27 NTU, **e,** 30 NTU, and **f,** 33 NTU.

## Supplementary Section S7

## Ship model imaging

Photographs of the metallic ship model and a direct optical image acquired in turbid water are provided in Fig. S7a-b. During LuDAR imaging, the model was slightly tilted, with the bow facing the scanning system.

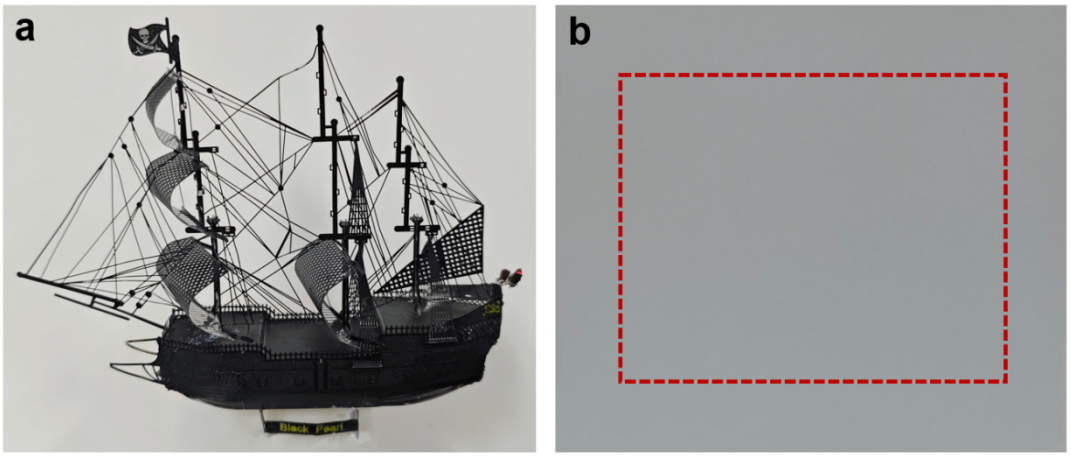


**Fig. S7 | Visual documentation of the ship model experiment. a,** Photograph of the metallic ship model. **b,** Direct optical camera image acquired in turbid water (25 NTU) at a working distance of 50 cm.